THE JOURNAL OF PHYSICAL CHEMISTRY C
A JOURNAL OF THE AMERICAN CHEMICAL SOCIETY

pubs.acs.org/JPCC
Article

Unraveling the Effect of Rh Isolation on Shallow d States of Gallium−Rhodium Alloys

Tzung-En Hsieh,* Sven Maisel, Haiko Wittkämper, Johannes Frisch, Julien Steffen, Regan G. Wilks, Christian Papp, Andreas Görling, and Marcus Bär*

Cite This: J. Phys. Chem. C 2023, 127, 20484−20490

ABSTRACT: In this study, we report the electronic and chemical structure of supported GaRh alloys as model systems for the active phase in supported catalytically active liquid metal solutions (SCALMS). We prepared a series of gallium−rhodium samples with different Rh contents and tracked the evolution of the sample topography and surface electronic structure via photoemission spectroscopy in combination with ab initio calculations and electron microscopy. Our results reveal a characteristic shift of the Rh 3d core levels and narrowing and shifting of the Rh 4d derived band with decreasing Rh content. Calculations show that these spectroscopic observations can be explained by the coexistence of isolated Rh atoms in random GaRh alloys and GaRh intermetallic compounds (IMCs). These results contribute to an enhancement of the fundamental understanding of the electronic surface structure of GaRh alloys, which is crucially required for apprehending and thus further exploiting the improved catalytic activity of GaRh SCALMS.

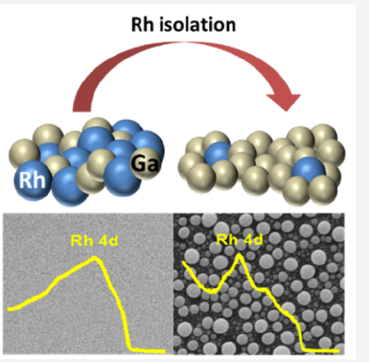

INTRODUCTION

Rhodium-containing bimetallic materials have been shown to be efficient catalysts for various thermocatalytic reactions, e.g., steam reforming as well as hydrogenation and dehydrogenation reactions.[1−3] In recent years, a new class of bimetallic catalysts based on diluted active sites in a liquid metal matrix, also known as supported catalytically active liquid metal−solution (SCALMS), has been developed for catalytic organic dehydrogenation reactions.[4−8] GaRh alloys with low Rh contents have proven promising as SCALMS for propane dehydrogenation with high productivity, selectivity, and long-term stability.[9,10] In recent studies, more fundamental insights into the migration phenomena and the chemical structure of Rh within GaRh alloys were reported.[11,12] In the SCALMS concept, Rh is thought to be highly isolated in the Ga matrix. Then, at the operating conditions, liquid Ga prevents the aggregation of Rh atoms and provides a dynamic environment which is expected to allow Rh atoms to migrate between bulk and surface within the SCALMS.[11] It is expected that such an isolated Rh exhibits a chemical and electronic structure significantly different from pristine Rh bulk.[13] The same trend has been observed for GaPd intermetallic compounds (IMCs), AgCu alloys, and Pt diluted catalysts as well.[14−17]

According to previous studies, the surface electronic structure of the bimetallic catalysts plays a significant role in tuning the adsorption energy.[18−20] Furthermore, experiments and theory show a strong correlation of the coupling strength between adsorbents and adsorbates and catalytic reactivity.[21−23] The site isolation of e.g. Rh in a Ga matrix results in a narrowing of the d band interpreted to be representing a free-atom-like state.[14] Based on the established Newns−Anderson−Grimley adsorption model[24−26] and the work from Nørskov et al.,[19,21,22] the narrowed d states alter the interaction of catalytic surface and adsorbates, presumably enhancing catalytic performance. However, the chemical and electronic structure of the free-atom-like Rh in GaRh SCALMS has not yet been reported. Thus, examining the electronic structure of Rh-isolated GaRh alloys experimentally is the missing crucially required next step for further understanding the origin of higher reactivity of GaRh SCALMS compared to conventional catalysts.[9,10,14,24−26]

METHODS

Materials and Sample Preparation. Gallium (powder) was purchased from Sigma-Aldrich/Alfa Aesar (99.99%), and rhodium (wire) was purchased from Aldrich (99.95%). The GaRh alloy samples were prepared via physical vapor deposition (PVD). A SPEC EBE-4 e-beam evaporator was used for deposition. All samples were prepared in ultrahigh vacuum (UHV) at a base pressure <1 × 10^{-8} mbar by codeposition of Ga and Rh on a natively oxidized silicon wafer (SiO_x/Si). Substrates were annealed to 500 °C to clean the surface and desorb water before deposition. During deposition,

Received: June 28, 2023
Revised: September 6, 2023
Published: October 5, 2023

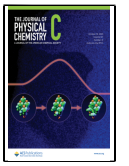

https://doi.org/10.1021/acs.jpcc.3c04350
J. Phys. Chem. C 2023, 127, 20484−20490

the substrate was kept at room temperature. The deposition rate was determined by a quartz crystal microbalance. Rh was evaporated using a 1 mm thick wire with an evaporation rate of 0.1−1 Å/min, and Ga was evaporated from a BN crucible with an evaporation rate of 1−8 Å/min, aiming at a total nominal thickness of 30 nm. By varying the evaporation rates, GaRh samples with nominal Rh contents of 0, 1, 4, 20, 50, 80, and 100 at. % have been prepared. After deposition, samples were transferred to the analysis chamber for photoemission measurements without breaking UHV conditions.

Scanning Electron Microscopy. Selected samples were examined by scanning electron microscopy (SEM) measurements using a Hitachi S 4100. For this, the sample to be studied is transferred under ambient conditions from the sample preparation chamber to the SEM setup. The SEM images are processed via ImageJ for particle size distribution. 200 particles in one SEM image were selected for the size distribution calculation.

Photoemission Spectroscopy. X-ray (XPS) and ultraviolet (UPS) photoelectron spectroscopy measurements were conducted using a nonmonochromatized Mg Kα (1253.56 eV, Specs XR 50) and He II (40.8 eV, Prevac UVS 40A2) excitation source, respectively. The photoelectrons were detected with a Scienta Argus CU electron analyzer. The pass energy for the core level detail spectra measurements was set to 20 eV, resulting in an experimental energy resolution of approximately 0.9 eV for the Mg Kα source. For the He II measurements, the pass energy was set to 4 eV, resulting in an energy resolution of approximately 0.1 eV. The total energy resolution was determined from the width of the Fermi edge of a clean polycrystalline Au sample. The binding energy (BE) scale of the measured core level and valence band spectra are referenced to the Fermi edge (at BE = 0 eV) of a clean polycrystalline Au sample. The XPS data were sequentially fitted and quantified by Winspec (LISE, Université de Paix, Namur) using Doniach−Sunjich for metallic species and Voigt for the nonmetallic species constraining the width of the peaks (and for the Ga 3d fit also the doublet separation) to be the same for a specific core level within the whole data set. The fitting results of Ga 3d (first fit the sum of $3d_{3/2}$ and $3d_{5/2}$ by the Doniach−Sunjich doublet profile and then only take the $3d_{5/2}$ contribution into account) and Rh $3d_{5/2}$ core level peaks are used for quantification. The Rh concentration is calculated by the following equations:

$$\frac{Rh}{Ga} = \frac{I_{Rh}/\sigma_{Rh}}{I_{Ga}/\sigma_{Ga}} \times \frac{\mathrm{IMFP}_{Ga}}{\mathrm{IMFP}_{Rh}}$$

$$[Rh] = \frac{\frac{Rh}{Ga}}{1 + \frac{Rh}{Ga}} \times 100 \text{ at. \%}$$

where I_{Ga} and I_{Rh} denote the peak area of Ga $3d_{5/2}$ and Rh $3d_{5/2}$ core level peaks. The applied photoionization cross section (σ) of Ga $3d_{5/2}$ and Rh $3d_{5/2}$ core levels are 0.161 and 1.92 arbitrary units, respectively.[27−29] The inelastic mean free path (IMFP) of Ga $3d_{5/2}$ and Rh $3d_{5/2}$ is 21.0 and 17.2 Å, respectively.[30−32] The fits of the Ga $3d_{5/2}$ and Rh $3d_{5/2}$ core level peaks are shown in Figures S1 and S2. The nominal and XPS derived compositions are compared in Figure S3 and Table S2.

Computational Details and Models. Ga_xRh_y IMCs and SCALMS model systems were further investigated using density-functional theory (DFT) as implemented in the Vienna Ab Initio Simulation Package (VASP). The projector augmented wave (PAW) method was applied to represent the atomic cores in conjunction with a plane wave basis set with a kinetic energy cutoff of 400 eV.[33−35] The electron exchange correlation was treated using the generalized gradient approximation (GGA) in the form of the functional developed by Perdew, Burke, and Ernzerhof (PBE).[36]

Known solid Ga_xRh_y IMCs with varying Rh content were considered,[37] namely $GaRh_3$, GaRh, $Ga_{17}Rh_{10}$, Ga_3Rh, Ga_9Rh_2, $Ga_{21}Rh_4$, and $Ga_{16}Rh_3$ (see Table S1). As the structure of the GaRh IMCs generated in the experiments remains mostly unknown, we additionally created solid random alloys by taking an fcc-Rh bulk cell (15.6 × 15.6 × 15.6 Å^3) containing 256 atoms and randomly exchanging a certain number of Rh atoms through Ga (10, 20, 30, 40, 50, 60, 70, 80, 90, and 95 at. % Ga). Both lattice constants and atomic positions were relaxed in geometry optimizations until the forces on all atoms were smaller than 10^{-3} and 10^{-2} eV/Å for known IMCs and random GaRh alloys, respectively. A first-order Methfessel−Paxton smearing with a width of 0.2 eV was used for geometry optimizations, and only the Γ point was sampled.[38] The convergence criterion for the electronic SCF was set to 10^{-8} eV. The number of k points for the sampling of the first Brillouin zone is given in Table S1 for all known GaRh IMCs investigated here together with the space group and calculated as well as experimental lattice constants.

In addition, liquid SCALMS slab models were generated in an ab initio molecular dynamics (AIMD) run using systems with 5 at. % Rh (i.e., $Ga_{171}Rh_9$ in a tetragonal unit cell with dimensions: 12.69 × 12.69 × 38.00 Å^3). At least 12 Å of vacuum was added in direction perpendicular to the surface to decouple periodic images. A constant temperature, constant volume (NVT) ensemble was sampled using a Nosé−Hoover thermostat at a temperature of 823 K using a time step of 10 fs with a total simulation time of 400 ps.[39] A Verlet algorithm was used to solve the equations of motion. Furthermore, a Fermi smearing was employed with a smearing width corresponding to the temperature conditions and the cutoff energy was lowered to 300 eV.[40] Γ-containing 2 × 2 × 1 k point meshes were generated for the surface slab models, and energy conservation during the AIMD run was ensured by an SCF convergence criterion of 10^{-7} eV. Bader charges were evaluated using all-electron charge densities.[41,42] Furthermore, larger k point meshes were used for electronic density of states (DOS) calculations for all systems together with a tetrahedron smearing with Blöchl corrections.[43] The center of the Rh 4d band ε_d was computed as $\varepsilon_d = \int x\rho(x)\,dx / \int \rho(x)\,dx$ with the electronic DOS distribution $\rho(x)$.

Core level (CL) binding energies for the Rh 3d core levels were computed in initial state (IS) and final state (FS) approximation as described in detail elsewhere.[13] In these calculations, larger unit cells with cell lengths greater than at least 13 Å in all directions were constructed in order to prevent interactions between the periodic images of the generated core holes. Moreover, the screening of the core electrons is not included in calculations within the PAW approximation. This introduces errors in the absolute binding energies which are, however, expected to cancel when core level shifts (CLS) are calculated; i.e., the difference to a reference system is considered, in this case pure Rh.

https://doi.org/10.1021/acs.jpcc.3c04350
J. Phys. Chem. C 2023, 127, 20484−20490

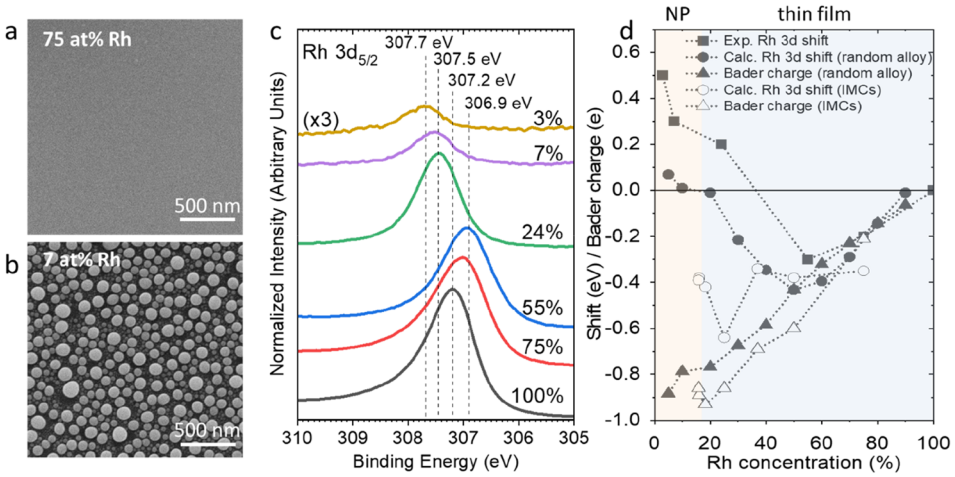

Figure 1. SEM images (top view) of GaRh samples containing (a) 75 at. % and (b) 7 at. % of Rh. (c) XPS (Mg Kα) Rh $3d_{5/2}$ detail spectra of GaRh samples with Rh/(Rh + Ga) surface contents decreasing from 100 to 3 at. % as derived by XPS measured at room temperature (see Figures S1−S3 for more details). The Rh $3d_{5/2}$ spectrum of GaRh containing 3 at. % Rh is magnified by a factor of 3. (d) Comparison of experimentally derived (squares) and calculated Rh 3d core level shifts (circles) and Bader charges on Rh atoms (triangles) for GaRh random alloys (closed symbols) and IMCs (open symbols) with Rh/(Rh + Ga) contents varying between 5 and 90 at. %. In (d), the samples with thin film and nanoparticle (NP) morphology are shown in the blue and red area, respectively. All Rh 3d core level shifts and Bader charge values are plotted relative to the respective value of the 100% Rh sample (0 eV).

RESULTS AND DISCUSSION

We present detailed ultraviolet and X-ray photoelectron spectroscopy (UPS/XPS) measurements of physical vapor deposited GaRh alloys on SiO_x/Si supports with Rh concentrations decreasing from 100 to 3 at. % (derived by XPS; see the Figures S1−S3) as model systems for GaRh SCALMS. We support these studies with scanning electron microscopy (SEM) and density functional theory (DFT) analysis. SEM images show that Rh-rich (e.g., 75 at. % Rh containing) GaRh alloys form a closed film (Figure 1a). As the Rh content decreases, a morphological transition to nanoparticles occurs (Figures 1b and S4). This dewetting phenomenon has been similarly observed in previous studies and causes a wide distribution of particle sizes. The GaRh alloys with, e.g., 7 at. % Rh form particles with a bimodal distribution of diameters which range in size from 10 to 120 nm with apparent maxima near 30 and 85 nm (Figures 1b and S5).[4,11,44] A similar size distribution is observed for the GaRh with 3 at. % Rh and the pure Ga sample (not shown); detailed microscopic studies of similar samples can be found in refs 9 and 11. These morphological variations are also corroborated by the XPS data (see discussion in conjunction with Figures S6 and S7). An impact on the chemical environment is evident from the binding energy (BE) changes observed for the Rh 3d core level peak with varying Rh concentrations (Figure 1c). For the 100 at. % Rh reference sample, the Rh $3d_{5/2}$ BE is 307.2 eV, similar to previously reported values of metallic Rh films.[45,46] As the Rh content decreases from 100 to 55 at. %, the BE shifts by 0.3 eV to lower values. As the Rh content further decreases to 3 at. %, the trend reverses, resulting in a 0.8 eV core level shift in the opposite direction, i.e., to higher BE. Comparing SEM images and XPS shifts, the most drastic morphology changes (the transition from film to particle topography; see Figures 1a,b and S4) occur when Rh is decreased from 24 down to 7 at. %, but the Rh $3d_{5/2}$ BE is largely insensitive to this difference, with only a 0.1 eV core level shift, effectively excluding topography (e.g., changing surface−volume ratio) as the underlying reason for the observed BE shifts. A detailed fit analysis of the Rh 3d line (see Figure S2) also excludes a partial Rh oxidation as explanation for the observed Rh 3d core level shifts.

To explain the observed nonmonotonous Rh $3d_{5/2}$ BE evolution, DFT calculations are employed to gain a deeper understanding of the origin of changes in chemical and electronic structure due to Rh isolation. Density of states (DOS), Rh core level shifts, and Bader charges on Rh atoms were calculated for reported GaRh intermetallic compounds (IMCs), random alloys, and liquid SCALMS (see the Supporting Information for details).[11,13,41,42,47] Figure 1d compares the experimentally derived Rh 3d BE shift (squares) to the DFT derived Rh 3d BE shifts (circles) and Bader charges (triangles) calculated for GaRh random alloys and known IMCs. A more detailed description of the calculated results can be found in conjunction to the discussion of Figure S8. The computed Bader charge values show a linear trend describing an increasing negative charge density at the Rh atoms with decreasing Rh concentration (Figure 1d, triangles) for both the GaRh random alloys and IMCs. This negative charge density is explained by a charge transfer from Ga to Rh. In a purely initial state picture of the photoemission process, additional negative charge would result in a core level shift to lower binding energy compared to a neutral reference due to the increased electron repulsion. As a result, the calculated linear increase of Bader charge would cause a continuous shift to a lower binding energy rather than the back-and-forth shift that we observed experimentally (Figure 1d, squares). However, in a more general picture of the photoemission process, the peak shape and position are influenced both by the local charge density at atoms (initial state) and by relaxation/screening of core holes formed during photoemission process (final state).[48−50] We conclude that for higher Rh concentrations from 100 to 55 at. %, the observed core level shifts are dominated by the initial state effect, namely the negative charge transfer from Ga to Rh, which results in negative binding energy shifts compared to metallic Rh as described above. For Rh concentrations below 55 at. % Rh, it appears

https://doi.org/10.1021/acs.jpcc.3c04350
J. Phys. Chem. C 2023, 127, 20484−20490

that final state effects begin to dominate, and a related shift to positive binding energies is observed for GaRh random alloys (Figure 1d, closed circles). Note that the IMC calculation results show a BE shift that is rather independent of the Rh content (Figure 1d, open circles). In summary, the evolution of the Rh 3d BE shift calculated for the GaRh random alloys agrees very well with the experimentally derived BE trend (Figure 1d, closed squares); i.e., a shift to lower BE until the Rh content decreases to 50 at. % followed by a positive BE shift for lower Rh contents. Even though the Rh 3d BE shift of random alloys is consistent with the trend of the experimental data, it has to be noted that the formation of IMCs such as $Ga_{21}Rh_4$ and $Ga_{16}Rh_3$ was observed by transmission electron microscopy as crystalline precipitates inside (mostly amorphous) GaRh particles in previous studies.[9,11] Thus, it would be expected that the GaRh alloys investigated in this study also contain some contribution from IMCs; most likely the probed sample volume is a mixture of crystalline (IMC-like) precipitates and amorphous (random alloy-like) GaRh material; see also the discussion in conjunction with Figure 3.

As a further probe of the chemical and electronic structure, UPS measurements were performed on the GaRh alloys, and they offer clear validation of the theoretical modeling as well as the inferences regarding the mixed presence of IMC and amorphous (i.e., random alloy) phases. For all measured UPS spectra in Figure 2a, a clear Fermi edge is observed indicating

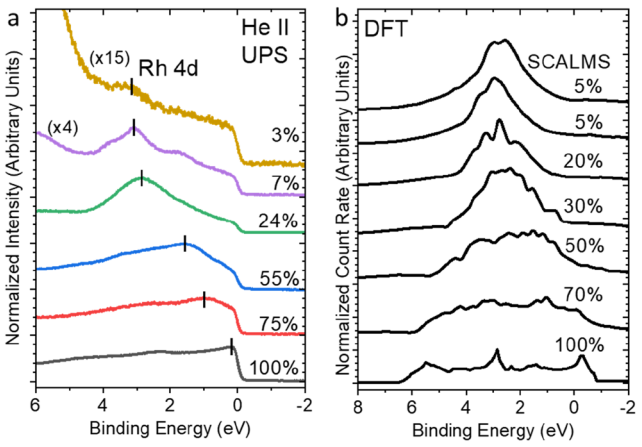

Figure 2. (a) Room temperature UPS (He II) spectra of GaRh samples with Rh/(Rh + Ga) ratios between 100 and 3 at %. (b) DFT calculated projected electronic DOS of Rh d-band states for GaRh random alloys with Rh contents decreasing from 100 to 5 at. % and GaRh SCALMS with 5 at. % Rh (topmost spectrum). The UPS spectra of the GaRh samples with 3 and 7 at. % Rh are magnified by a factor of 4 and 15, respectively. The highest spectral intensity related to Rh d-band derived states is indicated by vertical lines in (a).

the metallic nature of the sample. When moving from the pure Rh reference to the GaRh alloy with a Rh content of 75 at. %, the formation of a (broad) feature at around 1 eV BE can be observed (highlighted by a vertical line in Figure 2a) that is characteristic of the Rh 4d derived valence states. This feature narrows and shifts to a higher BE with decreasing Rh concentration (Figure 2a). In the measurement of the GaRh sample with 7 at. % Rh content the feature centers around 3 eV BE and has developed a complex spectral signature. When the Rh content is further reduced to 3 at. %, it becomes challenging to evaluate the feature's spectral appearance due to insufficient signal-to-noise ratio of the small Rh 4d derived contribution on spectral background dominated by Ga DOS.

The narrowing and shift of the Rh 4d derived signal to higher BE are also observed in the DFT calculated projected DOS (PDOS) of Rh d-band valence states for random GaRh alloys in Figures 2b and S9b. Note that the DOS of GaRh alloys in the presented energy region is dominated by Rh 4d derived contribution (Figure S10). For the calculated PDOS of the random GaRh alloy with 5 at. % Rh, a narrow Rh 4d state is found at around 3 eV, well reproducing energy position and spectral shape of the Rh 4d derived feature in the UPS spectrum of the GaRh alloys with 7 at. % Rh (see Figure 2a). Based on the used atomic structures for the DFT calculations, it is clear that (in this Rh concentration regime) Rh atoms are fairly distant from each other; i.e., the distance is more than 1 bridging atom.[11] Therefore, the distinct feature in the measured VB at 3 eV BE can be attributed to a similar isolated coordination environment of Rh atoms to that in the DFT calculations. Because GaRh alloys with Rh concentrations below 4 at. % as compared to alloys with higher Rh content are reported to have a higher productivity in e.g. propane dehydrogenation reaction,[9] this suggests that this isolated Rh coordination is beneficial for catalytic performance. According to the reported relationship between the electronic structure of active sites and bonding strength between catalyst and adsorbates,[21,22,S1] the Rh 4d band shift and narrowing (see UPS spectra in Figure 2a) may result in an altered bonding strength between Rh sites and adsorbates within the reaction pathway of propane dehydrogenation. This could be considered as a reason for the observed improved reactivity of GaRh SCALMS compared to Rh/AlO_x catalysts.[9,10] For corroboration, the calculated Rh PDOS of a (liquid) GaRh SCALMS with 5 at. % Rh content (see discussion in conjunction to Figure S9 for more context) is shown in Figure 2b (although, it must be noted that these conditions were not reproduced in the XPS/UPS measurements). The spectral shape and BE position are very similar to the PDOS calculated for the corresponding (solid) random GaRh alloy with 5 at. % Rh, indicating that the effect of liquefying the Ga host matrix on the electronic structure is negligible compared to the Rh isolation. This let us speculate that the UPS spectra shown for GaRh alloys with low (i.e., SCALMS relevant) Rh contents in Figure 2a are indeed representative of the electronic structure of GaRh SCALMS.

To further establish the spectroscopic fingerprint of isolated Rh d-band derived sites in the valence band objectively, we evaluate which calculated Rh PDOS possibly contributes to the measured UPS spectra; principal component analysis (PCA) of the experimental derived data set is performed (see details in the corresponding section of the Supporting Information) to evaluate the number of distinct contributions to the data set and further to use target transformation to evaluate the possible presence of spectral signatures resembling the calculated Rh PDOS. The full set of the target transformation of (i) the GaRh random alloys, (ii) the IMCs, and (iii) the SCALMS is shown in Figures S13−S15. The target transformation of the calculated PDOS for the (solid) random GaRh alloy and (liquid) SCALMS both with 5 at. % Rh content results in the lowest χ^2 values. The very similar χ^2 values for the GaRh random alloy and SCALMS confirm a negligible impact of Ga liquefaction on the electronic structure. Because the UPS measurements are conducted at room temperature rather than at SCALMS relevant conditions, we

https://doi.org/10.1021/acs.jpcc.3c04350
J. Phys. Chem. C 2023, 127, 20484−20490

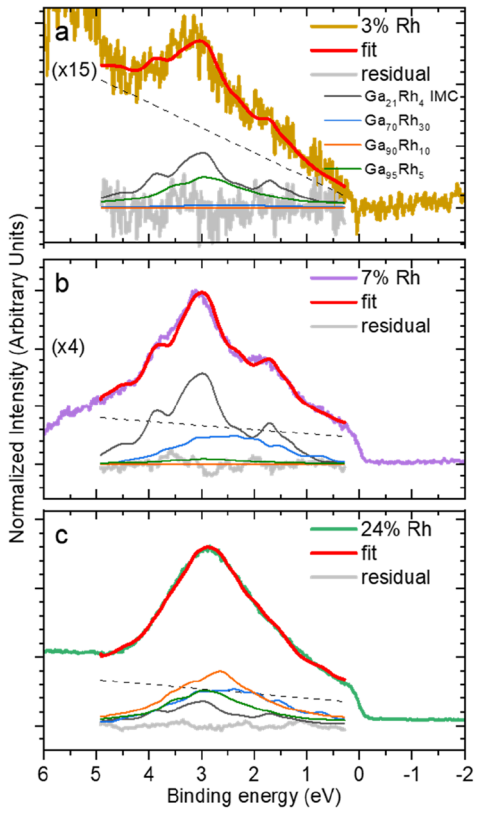

Figure 3. Room temperature UPS (He II) spectra of GaRh alloys with 3 at. % Rh (a), 7 at. % Rh (b), and 24 at. % Rh (c) from which a suitably scaled Ga reference spectrum was subtracted (see Figure S11 for details). The "fit" curve represents the results of a linear combination of calculated PDOS, which are included in each panel, scaled according to their respective contributions to the fit. The dashed lines have slope and offset optimized as part of the LCA and are included to account for the presence of the Fermi edge, secondary electrons, and other background effects. The range of the fit and components shown correspond to the range used for the fit. The intensity axis is common in all three panels; scaling factors are applied in panels a and b as indicated.

expect that the electronic structure of the GaRh alloys to be better described by the random alloy instead of the SCALMS model. This is in agreement with the BE shift found by these calculations to be consistent with the experimentally derived Rh 3d shift discussed above in conjunction with Figure 1d. Another remarkable result of the target transformation is the excellent reproduction of the feature-rich Rh PDOS calculated for the $Ga_{21}Rh_4$ IMC (Figure S14); the strong agreement in relative positions and intensities of all peaks and shoulders (especially the multiple well matching features at −1.7, −3.0, and −3.9 eV) provides compelling evidence that a spectral signature resembling the calculated $Ga_{21}Rh_4$ IMC Rh PDOS is presumably present in the measured data set. These results confirm the coexistence of random alloy and IMC phases which was suggested based on microscopy results.[9,11] Furthermore, a linear combination analysis (LCA) shows that the ratio of these two contributions (random alloy and IMC) seems to change for GaRh alloys with varying Rh content. This change is illustrated in Figure 3 which shows the measured UPS spectra for the GaRh alloys with 3, 7, and 24 at. % Rh can be reproduced by LCA of calculated Rh PDOS of the $Ga_{21}Rh_4$ IMC and representative random alloys (relative spectral weights are given in Table S3). The PDOS of the random alloys were initially selected due to the low χ^2 values of the target transformation (see Figure S13) and were refined during the LCA process to produce adequate fits using the minimum number of individual contributions—this procedure is meant to illustrate the IMC Rh PDOS contribution and how it changes, in a relative sense, with changing Rh content rather than claiming to quantitatively describe this complex picture fully. The relatively broad and featureless natures of the measured spectra and calculated Rh PDOS for higher Rh contents mean that this process cannot provide clear evidence for the presence or absence of particular random alloy configurations. We therefore stress that the random alloy PDOS contributions should be understood to represent less ordered alloy constituents in general in the data sets. Attempts to perform LCA on the spectra with higher Rh contents were largely unsuccessful (and are not included), which we attribute to increasingly mismatched broadening in the UPS spectra and calculated PDOS. Subject to the strict constraints described above, the LCA indicates higher IMC contributions to 7 at. % Rh containing GaRh samples (approximately 65 ± 10% spectral weight based on numerous fitting attempts) compared to the 3 and 24 at. % Rh samples (approximately 15 ± 10% spectral weight based on numerous fitting attempts). The lower IMC contribution within 3 at. % Rh sample can be attributed to the highly diluted Rh in the Ga matrix, reducing the possibility of crystallization. On the other hand, the similarly lower IMC presence in 24 at. % Rh sample can be explained by the close-packed thin film morphology which also limits the IMC growth due to less mobile Rh atoms.[47] In summary, these LCA results reveal a significant change in the presence of different GaRh phases while tuning the Rh concentration.

CONCLUSION

We present a combination of X-ray/UV photoemission, SEM, and DFT investigations on the electronic and chemical structure and topography of GaRh alloys for Rh contents varying from 100 to 3 at. %. The topography changes significantly from being best described by closed thin films for samples with a Rh content ≥24 at. % to being indicative for the formation of nanoparticles with a bimodal size distribution for GaRh alloys with Rh contents up to 7 at. %. In XPS we observe a shift of the Rh 3d photoemission line to lower BE until the Rh content decreases to 55 at. % followed by a positive BE shift for lower Rh contents. Calculations for random GaRh alloys show that the complex Rh 3d core level shifts can be explained by two competing effects, increasing negative charging on the Rh atoms and reduced screening of the generated core hole, which induce a back-and-forth shift in core level binding energies when moving from high to low Rh content. UPS also reveals a shift and a narrowing of the Rh 4d derived spectral feature in the valence band. DFT results indicate that the origin of the d-band shifting and narrowing is the isolation of Rh atoms within the Ga matrix. Such a narrowed and shifted Rh d-band may result in an enhanced coupling strength between adsorbates and Rh sites during the catalytic process, presumably explaining the improved catalytic performance of GaRh SCALMS.

PCA and subsequent LCA of the Rh PDOS calculated for random GaRh alloys and known IMCs prove the coexistence of random alloy and IMC phases within the studied GaRh samples. While the electronic structure of alloys with Rh

https://doi.org/10.1021/acs.jpcc.3c04350
J. Phys. Chem. C 2023, 127, 20484−20490

contents up to 7 at. % is dominated by spectral features corresponding to Rh PDOS of IMCs, for GaRh alloys with 3 and 24 at. % Rh contents, we find the electronic structure to be dominated by Rh PDOS from random alloys. The fact that the Rh isolation effect on the electronic structure of the GaRh alloys is significantly more pronounced than the effect of liquefying the Ga matrix (e.g., when going from solid IMCs to liquid SCALMS) justifies considering this study on GaRh alloys as a valid model system for the active phase in SCALMS, and thus the presented results represent a step toward fully apprehending the improved catalytic activity of GaRh SCALMS.

■ ASSOCIATED CONTENT

Supporting Information

The Supporting Information is available free of charge at https://pubs.acs.org/doi/10.1021/acs.jpcc.3c04350.

Details in DFT calculation, SEM characterizations, description of PCA and target transformation, additional XPS/UPS spectra and fitting results, tables showing quantified XPS fitting results (PDF)

■ AUTHOR INFORMATION

Corresponding Authors

Tzung-En Hsieh − *Department of Interface Design, Helmholtz-Zentrum Berlin für Materialien und Energie GmbH (HZB), 12489 Berlin, Germany;* orcid.org/0000-0003-1844-2635; Email: tzung-en.hsieh@helmholtz-berlin.de

Marcus Bär − *Department of Interface Design, Helmholtz-Zentrum Berlin für Materialien und Energie GmbH (HZB), 12489 Berlin, Germany; Department of Chemistry and Pharmacy, Friedrich-Alexander-Universität Erlangen-Nürnberg (FAU), 91058 Erlangen, Germany; Energy Materials In-situ Laboratory Berlin (EMIL), HZB, 12489 Berlin, Germany; Department X-ray Spectroscopy at Interfaces of Thin Films, Helmholtz Institute Erlangen-Nürnberg for Renewable Energy (HI ERN), 12489 Berlin, Germany;* orcid.org/0000-0001-8581-0691; Email: marcus.baer@helmholtz-berlin.de

Authors

Sven Maisel − *Department of Chemistry and Pharmacy, Friedrich-Alexander-Universität Erlangen-Nürnberg (FAU), 91058 Erlangen, Germany*

Haiko Wittkämper − *Department of Chemistry and Pharmacy, Friedrich-Alexander-Universität Erlangen-Nürnberg (FAU), 91058 Erlangen, Germany*

Johannes Frisch − *Department of Interface Design, Helmholtz-Zentrum Berlin für Materialien und Energie GmbH (HZB), 12489 Berlin, Germany; Energy Materials In-situ Laboratory Berlin (EMIL), HZB, 12489 Berlin, Germany*

Julien Steffen − *Department of Chemistry and Pharmacy, Friedrich-Alexander-Universität Erlangen-Nürnberg (FAU), 91058 Erlangen, Germany;* orcid.org/0000-0001-7933-9557

Regan G. Wilks − *Department of Interface Design, Helmholtz-Zentrum Berlin für Materialien und Energie GmbH (HZB), 12489 Berlin, Germany; Energy Materials In-situ Laboratory Berlin (EMIL), HZB, 12489 Berlin, Germany;* orcid.org/0000-0001-5822-8399

Christian Papp − *Department of Chemistry and Pharmacy, Friedrich-Alexander-Universität Erlangen-Nürnberg (FAU), 91058 Erlangen, Germany; Physical and Theoretical Chemistry, Freie Universität Berlin, 14195 Berlin, Germany;* orcid.org/0000-0002-1733-4387

Andreas Görling − *Department of Chemistry and Pharmacy, Friedrich-Alexander-Universität Erlangen-Nürnberg (FAU), 91058 Erlangen, Germany;* orcid.org/0000-0002-1831-3318

Complete contact information is available at: https://pubs.acs.org/10.1021/acs.jpcc.3c04350

Notes

The authors declare no competing financial interest.

■ ACKNOWLEDGMENTS

The authors gratefully acknowledge the funding by the Deutsche Forschungsgemeinschaft (DFG, German Research Foundation)—Project-ID 431791331—CRC 1452 (CLINT Catalysis at Liquid Interfaces). The authors also thank Ms. Carola Klimm at Department Solution-Processing of Hybrid Materials and Devices in HZB for helpful assistance in the SEM measurements.

■ REFERENCES

(1) Liu, H.; Zhou, C.; Li, W.; Li, W.; Qiu, M.; Chen, X.; Wang, H.; Sun, Y. Ultralow Rh Bimetallic Catalysts with High Catalytic Activity for the Hydrogenation of N-Ethylcarbazole. *ACS Sustain. Chem. Eng.* **2021**, *9*, 5260−5267.

(2) Park, J. Y.; Zhang, Y.; Joo, S. H.; Jung, Y.; Somorjai, G. A. Size Effect of RhPt Bimetallic Nanoparticles in Catalytic Activity of CO Oxidation: Role of Surface Segregation. *Catal. Today* **2012**, *181*, 133−137.

(3) Kugai, J.; Subramani, V.; Song, C.; Engelhard, M. H.; Chin, Y.-H. Effects of Nanocrystalline CeO_2 Supports on The Properties and Performance of Ni−Rh bimetallic Catalyst for Oxidative Steam Reforming of Ethanol. *J. Catal.* **2006**, *238*, 430−440.

(4) Taccardi, N.; Grabau, M.; Debuschewitz, J.; Distaso, M.; Brandl, M.; Hock, R.; Maier, F.; Papp, C.; Erhard, J.; Neiss, C.; et al. Gallium-Rich Pd−Ga Phases as Supported Liquid Metal Catalysts. *Nat. Chem.* **2017**, *9*, 862−867.

(5) Kettner, M.; Maisel, S.; Stumm, C.; Schwarz, M.; Schuschke, C.; Görling, A.; Libuda, J. Pd-Ga Model SCALMS: Characterization and Stability of Pd Single Atom Sites. *J. Catal.* **2019**, *369*, 33−46.

(6) Wolf, M.; Raman, N.; Taccardi, N.; Horn, R.; Haumann, M.; Wasserscheid, P. Capturing Spatially Resolved Kinetic Data and Coking of Ga−Pt Supported Catalytically Active Liquid Metal Solutions during Propane Dehydrogenation In Situ. *Faraday Discuss.* **2021**, *229*, 359−377.

(7) Hohner, C.; Kettner, M.; Stumm, C.; Blaumeiser, D.; Wittkämper, H.; Grabau, M.; Schwarz, M.; Schuschke, C.; Lykhach, Y.; Papp, C.; et al. Pt−Ga Model SCALMS on Modified HOPG: Thermal Behavior and Stability in UHV and under Near-Ambient Conditions. *J. Phys. Chem. C* **2020**, *124*, 2562−2573.

(8) Grabau, M.; Krick Calderón, S.; Rietzler, F.; Niedermaier, I.; Taccardi, N.; Wasserscheid, P.; Maier, F.; Steinrück, H.-P.; Papp, C. Surface Enrichment of Pt in Ga2O3 Films Grown on Liquid Pt/Ga Alloys. *Surf. Sci.* **2016**, *651*, 16−21.

(9) Raman, N.; Maisel, S.; Grabau, M.; Taccardi, N.; Debuschewitz, J.; Wolf, M.; Wittkämper, H.; Bauer, T.; Wu, M.; Haumann, M.; et al. Highly Effective Propane Dehydrogenation Using Ga−Rh Supported Catalytically Active Liquid Metal Solutions. *ACS Catal.* **2019**, *9*, 9499−9507.

(10) Wolf, M.; Raman, N.; Taccardi, N.; Haumann, M.; Wasserscheid, P. Coke Formation during Propane Dehydrogenation

over Ga−Rh Supported Catalytically Active Liquid Metal Solutions. *ChemCatChem* **2020**, *12*, 1085−1094.
(11) Wittkämper, H.; Maisel, S.; Wu, M.; Frisch, J.; Wilks, R. G.; Grabau, M.; Spiecker, E.; Bär, M.; Görling, A.; Steinrück, H.-P.; Papp, C. Oxidation Induced Restructuring of Rh−Ga SCALMS Model Catalyst Systems. *J. Chem. Phys.* **2020**, *153*, 104702.
(12) Bauer, T.; Maisel, S.; Blaumeiser, D.; Vecchietti, J.; Taccardi, N.; Wasserscheid, P.; Bonivardi, A.; Görling, A.; Libuda, J. Operando DRIFTS and DFT Study of Propane Dehydrogenation over Solid- and Liquid-Supported GaxPty Catalysts. *ACS Catal.* **2019**, *9*, 2842−2853.
(13) Wittkämper, H.; Hock, R.; Weißer, M.; Dallmann, J.; Vogel, C.; Raman, N.; Tacardi, N.; Haumann, M.; Wasserscheid, P.; Hsieh, T.-E.; et al. Isolated Rh Atoms in Dehydrogenation Catalysis. *Sci. Rep.* **2023**, *13*, 4458.
(14) Greiner, M. T.; Jones, T. E.; Beeg, S.; Zwiener, L.; Scherzer, M.; Girgsdies, F.; Piccinin, S.; Armbrüster, M.; Knop-Gericke, A.; Schlögl, R. Free-Atom-Like d States in Single-Atom Alloy Catalysts. *Nat. Chem.* **2018**, *10*, 1008−1015.
(15) Lai, W.-H.; Miao, Z.; Wang, Y.-X.; Wang, J.-Z.; Chou, S.-L. Atomic-Local Environments of Single-Atom Catalysts: Synthesis, Electronic Structure, and Activity. *Adv. Energy Mater.* **2019**, *9*, 1900722.
(16) Meng, G.; Zhang, J.; Li, X.; Wang, D.; Li, Y. Electronic Structure Regulations of Single-Atom Site Catalysts and Their Effects on the Electrocatalytic Performances. *Appl. Phys. Rev.* **2021**, *8*, No. 021321.
(17) Armbrüster, M.; Schlögl, R.; Grin, Y. Intermetallic Compounds in Heterogeneous Catalysis—A Quickly Developing Field. *Sci. Technol. Adv. Mater.* **2014**, *15*, No. 034803.
(18) Zhang, J.; Xu, W.; Liu, Y.; Hung, S.-F.; Liu, W.; Lam, Z.; Tao, H. B.; Yang, H.; Cai, W.; Xiao, H.; et al. In Situ Precise Tuning of Bimetallic Electronic Effect for Boosting Oxygen Reduction Catalysis. *Nano Lett.* **2021**, *21*, 7753−7760.
(19) Hammer, B.; Nørskov, J. K. Theoretical Surface Science and Catalysis—Calculations and Concepts. *Adv. Catal.* **2000**, *45*, 71−129.
(20) Rodriguez, J. A.; Goodman, D. W. The Nature of the Metal-Metal Bond in Bimetallic Surfaces. *Science* **1992**, *257*, 897−903.
(21) Zhang, J.; Vukmirovic, M. B.; Xu, Y.; Mavrikakis, M.; Adzic, R. R. Controlling the Catalytic Activity of Platinum-Monolayer Electrocatalysts for Oxygen Reduction with Different Substrates. *Angew. Chem., Int. Ed.* **2005**, *44*, 2132−2135.
(22) Nørskov, J. K.; Abild-Pedersen, F.; Studt, F.; Bligaard, T. Density Functional Theory in Surface Chemistry and Catalysis. *Proc. Natl. Acad. Sci. U. S. A.* **2011**, *108*, 937.
(23) Nilekar, A. U.; Mavrikakis, M. Improved Oxygen Reduction Reactivity of Platinum Monolayers on Transition Metal Surfaces. *Surf. Sci.* **2008**, *602*, L89−L94.
(24) Davison, S. G.; Sulston, K. W. Anderson-Newns-Grimley Model. In *Green-Function Theory of Chemisorption*; Davison, S. G., Sulston, K. W., Eds.; Springer Netherlands: Dordrecht, 2006; pp 45−74.
(25) Newns, D. M. Self-Consistent Model of Hydrogen Chemisorption. *Prhys. Rev.* **1969**, *178*, 1123−1135.
(26) Anderson, P. W. Localized Magnetic States in Metals. *Prhys. Rev.* **1961**, *124*, 41−53.
(27) Scofield, J. H. Hartree-Slater Subshell Photoionization Cross-Sections at 1254 and 1487 eV. *J. Electron Spectrosc. Relat. Phenom.* **1976**, *8*, 129−137.
(28) Trzhaskovskaya, M. B.; Nikulin, V. K.; Nefedov, V. I.; Yarzhemsky, V. G. Influence of nondipolar effects on the photoelectron angular distribution upon photoionization of 2p and 3d atomic shells. *Opt. Spectrosc.* **2004**, *96*, 765−773.
(29) Trzhaskovskaya, M. B.; Nefedov, V. I.; Yarzhemsky, V. G. Photoelectron Angular Distribution Parameters for Elements Z = 1 to Z = 54 in the Photoelectron Energy Range 100−5000 eV. *At. Data Nucl. Data Tables* **2001**, *77*, 97−159.
(30) Seah, M. P.; Dench, W. A. Quantitative Electron Spectroscopy of Surfaces: A Standard Data Base for Electron Inelastic Mean Free Paths in Solids. *Surf. Interface Anal.* **1979**, *1*, 2−11.
(31) Tanuma, S.; Powell, C. J.; Penn, D. R. Calculations of Electorn Inelastic Mean Free Paths. II. Data for 27 Elements over the 50−2000 eV Range. *Surf. Interface Anal.* **1991**, *17*, 911−926.
(32) Tanuma, S.; Powell, C. J.; Penn, D. R. Calculation of Clectron Inelastic Mean Free Paths (IMFPs) VII. Reliability of the TPP-2M IMFP Predictive Equation. *Surf. Interface Anal.* **2003**, *35*, 268−275.
(33) Kresse, G.; Furthmüller, J. Efficient Iterative Schemes for Ab Initio Total-Energy Calculations Using a Plane-Wave Basis Set. *Phys. Rev. B* **1996**, *54*, 11169−11186.
(34) Kresse, G.; Furthmüller, J. Efficiency of Ab-Initio Total Energy Calculations for Metals and Semiconductors Using a Plane-Wave Basis Set. *Comput. Mater. Sci.* **1996**, *6*, 15−50.
(35) Kresse, G.; Joubert, D. From Ultrasoft Pseudopotentials to the Projector Augmented-Wave Method. *Phys. Rev. B* **1999**, *59*, 1758−1775.
(36) Perdew, J. P.; Burke, K.; Ernzerhof, M. Generalized Gradient Approximation Made Simple. *Phys. Rev. Lett.* **1996**, *77*, 3865−3868.
(37) Jain, A.; Ong, S. P.; Hautier, G.; Chen, W.; Richards, W. D.; Dacek, S.; Cholia, S.; Gunter, D.; Skinner, D.; Ceder, G.; Persson, K. A. Commentary: The Materials Project: A Materials Genome Approach to Accelerating Materials Innovation. *APL Mater.* **2013**, *1*, No. 011002.
(38) Methfessel, M.; Paxton, A. T. High-Precision Sampling for Brillouin-Zone Integration in Metals. *Phys. Rev. B* **1989**, *40*, 3616−3621.
(39) Nosé, S. A Unified Formulation of the Constant Temperature Molecular Dynamics Methods. *J. Chem. Phys.* **1984**, *81*, 511−519.
(40) Mermin, N. D. Thermal Properties of the Inhomogeneous Electron Gas. *Prhys. Rev.* **1965**, *137*, A1441−A1443.
(41) Henkelman, G.; Arnaldsson, A.; Jónsson, H. A Fast and Robust Algorithm for Bader Decomposition of Charge Density. *Comput. Mater. Sci.* **2006**, *36*, 354−360.
(42) Tang, W.; Sanville, E.; Henkelman, G. A Grid-Based Bader Analysis Algorithm without Lattice Bias. *J. Phys.: Condens. Matter* **2009**, *21*, No. 084204.
(43) Blöchl, P. E.; Jepsen, O.; Andersen, O. K. Improved Tetrahedron Method for Brillouin-Zone Integrations. *Phys. Rev. B* **1994**, *49*, 16223−16233.
(44) Raman, N.; Wolf, M.; Heller, M.; Heene-Würl, N.; Taccardi, N.; Haumann, M.; Felfer, P.; Wasserscheid, P. GaPt Supported Catalytically Active Liquid Metal Solution Catalysis for Propane Dehydrogenation−Support Influence and Coking Studies. *ACS Catal.* **2021**, *11*, 13423−13433.
(45) Marot, L.; Schoch, R.; Steiner, R.; Meyer, E. Rhodium and Silicon System: I. Glassy Metallic Alloy Formation. *Nanotechnology* **2010**, *21*, 365706.
(46) Kibis, L. S.; Stadnichenko, A. I.; Koscheev, S. V.; Zaikovskii, V. I.; Boronin, A. I. XPS Study of Nanostructured Rhodium Oxide Film Comprising Rh4+ Species. *J. Phys. Chem. C* **2016**, *120*, 19142−19150.
(47) Anres, P.; Gaune-Escard, M.; Bros, J. P. Thermodynamics of the (Rh−Ga) System. *J. Alloys Compd.* **1998**, *265*, 201−208.
(48) Fuggle, J. C.; Campagna, M.; Zolnierek, Z.; Lässer, R.; Platau, A. Observation of a Relationship between Core-Level Line Shapes in Photoelectron Spectroscopy and the Localization of Screening Orbitals. *Phys. Rev. Lett.* **1980**, *45*, 1597−1600.
(49) Kleiman, G. G.; Landers, R. The Effect of Final State Screening Changes on Alloy Energy Shifts. *J. Electron Spectrosc. Relat. Phenom.* **1995**, *76*, 319−323.
(50) Aoki, T.; Ohno, K. Accurate Quasiparticle Calculation of X-Ray Photoelectron Spectra of Solids. *J. Phys.: Condens. Matter* **2018**, *30*, 21LT01.
(51) Zhu, B.; Lu, J.; Sakaki, S. Catalysis of Core-Shell Nanoparticle M@Pt (MCo and Ni) for Oxygen Reduction Reaction and its Electronic Structure in Comparison to Pt Nanoparticle. *J. Catal.* **2021**, *397*, 13−26.

https://doi.org/10.1021/acs.jpcc.3c04350
J. Phys. Chem. C 2023, 127, 20484−20490